Magnetized Plasma for Reconfigurable Subdiffraction Imaging

Shuang Zhang, Yi Xiong, Guy Bartal, Xiaobo Yin, and Xiang Zhang

Phys. Rev. Lett. **106**, 243901 — Published 13 June 2011

DOI: 10.1103/PhysRevLett.106.243901

Magnetized Plasma for Reconfigurable sub-diffraction-imaging

Shuang Zhang[1], Yi Xiong[1], Guy Bartal[1], Xiaobo Yin[1, 2] and Xiang Zhang[1, 2&]

1. 5130 Etcheverry Hall, Nanoscale Science and Engineering Center, University of California*, Berkeley, California 94720-1740, USA*

2. Materials Sciences Division, Lawrence Berkeley National Laboratory, 1 Cyclotron Road Berkeley, California 94720

Superlens capable of imaging beyond diffraction limits are normally made from metamaterials – artificially engineered materials with unconventional optical properties. In this Letter, we show that magnetized plasma with appropriately designed parameters supports nearly diffraction-less propagation of electromagnetic waves along the direction of the applied magnetic field, arising from their unbounded equi-frequency contour in the magnetized plasma. Such a unique feature can be utilized to construct sub-diffraction imaging devices, which is confirmed by detailed numerical investigations. Sub-diffraction imaging devices based on magnetic plasma do not require micro-fabrication normally entailed by construction of metamaterials, more importantly, they can be dynamically reconfigured by tuning the applied magnetic field or the plasma density, and therefore they represent a facile and powerful route for imaging applications.

PACS numbers: 42.25.Bs, 52.25.Xz, 78.20.Ci

[&] To whom correspondence should be addressed. E-mail: xiang@berkeley.edu

The progress in the field of metamaterials has shown many new striking physics [1, 2] that may lead to many important applications, including sub-diffraction imaging, slow light, and invisibility cloaking [3, 4, 5, 6]. Imaging beyond diffraction limit is of special importance because of many applications ranging from biological imaging in the optical regime, to magnetic resonance imaging (MRI) at the radio frequencies. It has been proposed that a negative index metamaterial slab is capable of magnifying the evanescent waves that carry the information of high spatial resolutions, and recovering the fine features of the object at the image plane [2]. Following this suggestion, imaging beyond diffraction limits has been experimentally realized from microwave to optical frequencies [3, 4, 7]. However, the spatial resolution of imaging using the negative index metamaterials is extremely sensitive to the presence of material loss, and therefore limiting their applications as practical super imaging devices.

Recently, it was shown that anisotropic media with mixed signs of permittivity tensor elements (the so called "indefinite" media) exhibit a very unique dispersion relation that supports hyperbolic equi-frequency contour (EFC), allowing the propagation of electromagnetic waves with very large wave vectors [8, 9, 10]. As a result, super fine features of the objects can be transported by propagating waves through the medium. In comparison with the negative index slab, the imaging through a hyperbolic medium is highly robust against the presence of material loss, therefore, it represents a more practical approach for sub-diffraction imaging. Artificial media with hyperbolic dispersion have been demonstrated recently in the form of metallic wires array, metal-dielectric multi-layers, and Swiss roll magnetic resonators [11, 12, 13, 14]. However, the fabrication of these media requires time consuming microfabrication procedures, and the

electromagnetic properties cannot be conveniently reconfigured in real time. Here we propose to employ magnetized plasma for achieving dynamically reconfigurable super-imaging at the radio, microwave and terahertz frequencies. With appropriate design, magnetized plasma supports unbounded EFC in a similar way as the hyperbolic medium, albeit with more complex dispersion features stemming from the breaking of time reversal symmetry due to the presence of magnetic field. The electromagnetic properties of magnetized plasma can be tuned by varying the external magnetic field or the density of the plasma, thus representing a very promising route towards a wide range of applications that requires real time reconfigurations.

The electromagnetic properties of a lossless plasma are described by Drude model, $\varepsilon_p = 1 - \frac{\omega_p^2}{\omega^2}$, where $\omega_p = \sqrt{\frac{Ne^2}{\varepsilon_0 m}}$ is the plasma frequency, N being the electron concentration. For electromagnetic waves with frequency below the plasma frequency, the plasma exhibits metallic-like properties and the waves cannot propagate through the plasma. Whereas under a strong external DC magnetic field, the electromagnetic properties of the plasma are modified in such a way that, they not only show direction dependent wave propagation (anisotropy), but also exhibit optical activity for electromagnetic waves propagating along the direction of the magnetic field. In a magnetized plasma, the electrons circle around the direction of the magnetic field at the cyclotron frequency, given as $\omega_c = \frac{eB}{m}$. As a result, the permittivity takes the form of a tensor [15],

$$\varepsilon = \begin{pmatrix} \varepsilon_1 & -i\varepsilon_2 & 0 \\ i\varepsilon_2 & \varepsilon_1 & 0 \\ 0 & 0 & \varepsilon_p \end{pmatrix} \qquad (1)$$

where $\varepsilon_1 = 1 + \frac{\omega_p^2}{\omega_c^2 - \omega^2}$, $\varepsilon_2 = \frac{\omega_p^2 \omega_c}{\omega(\omega_c^2 - \omega^2)}$ and $\varepsilon_p = 1 - \frac{\omega_p^2}{\omega^2}$. Notably, in the presence of an infinitely large applied magnetic field, the off-diagonal elements in Eq. (1) disappear, and the permittivity can be simply written as,

$$\varepsilon = \begin{pmatrix} 1 & 0 & 0 \\ 0 & 1 & 0 \\ 0 & 0 & 1 - \frac{\omega_p^2}{\omega^2} \end{pmatrix} \qquad (2)$$

According to Equation (2), a plasma under infinitely strong magnetic field exhibits the same electromagnetic properties as an uniaxial anisotropic medium. Depending on whether the frequency of the electromagnetic wave is above or below the plasma frequency, the EFC of the magnetized plasma can be either elliptical or hyperbolic. In particular, for the electromagnetic frequency well below the plasma frequency, the hyperbolic EFC exhibits very flat feature, which lays the foundation for applications such as hyperlens [11], and subwavelength endoscope [13].

However, in a realistic system, the magnitude of the magnetic field is always finite. Therefore, the off-diagonal elements in Eq. (1) still play an important role for determining the electromagnetic properties of the magnetized plasma. In the following, we will explore the potential of realistic magnetized plasma for sub-diffraction imaging applications. The dispersion relation of magnetized plasma is given as [15],

$$\tan^2\theta = -\frac{\varepsilon_p(n^2 - \varepsilon_R)(n^2 - \varepsilon_L)}{\varepsilon_1(n^2 - \varepsilon_X)(n^2 - \varepsilon_P)} \qquad (3)$$

where θ is angle formed between the wave vector and the applied magnetic field, n is the refractive index, $\varepsilon_{L(R)} = 1 - \frac{\omega_p^2}{\omega(\omega \mp \omega_c)}$, and $\varepsilon_X = \frac{\varepsilon_R \varepsilon_L}{\varepsilon_1}$. The dispersion given by Eq. (3) shows very rich features depending on the relative values of ω, ω_p and ω_c. Here we are only interested in the case where the electromagnetic frequency is far below the plasma frequency for the imaging purpose. We assume a realistic magnetized plasma system in which the plasma density is $1\times10^{12} cm^{-3}$ (corresponding to $\omega_p = 5.64\times10^{10} rad/s$) under an applied DC magnetic field ranging from 1 to 4 Tesla (T), with the corresponding cyclotron frequency ranging from $1.76\times10^{11} rad/s$ to $7.03\times10^{11} rad/s$. Since the collision frequency is normally in the megahertz scale [16], which is several orders of magnitude lower than the frequency of electromagnetic field of interest, it will be neglected in the subsequent investigation of EFCs of the magnetized plasma.

We first plot the critical parameters ε_R, ε_L, ε_P, and ε_X for the electromagnetic frequency below the plasma frequency at an applied magnetic field of 4T, in Fig. 1(a). The presence of magnetic field break the time reversal symmetry and lead to different dispersions for left handed (LH) and right handed (RH) circularly polarized electromagnetic waves propagating along the magnetic field, with refractive indices $\sqrt{\varepsilon_{L(R)}}$, which could be real even for the electromagnetic frequencies below the plasma frequency. The two modes become elliptically polarized for $0 < \theta < \pi/2$. At $\theta = \pi/2$, the LH and RH modes turn into ordinary and extraordinary modes, with polarization

parallel and perpendicular to the applied magnetic field, and refractive indices given by $\sqrt{\varepsilon_p}$ and $\sqrt{\varepsilon_X}$, respectively.

As shown by Fig. 1(a), for electromagnetic frequency below the plasma frequency, the LH mode exhibits a positive dielectric constant ($\varepsilon_L > 0$) for propagation along the applied magnetic field, and a negative dielectric constant ($\varepsilon_P < 0$) for propagation perpendicular to it, indicating an unbounded EFC for the LH mode. This is confirmed by the plots of EFCs for an electromagnetic frequency of 1 GHz (λ=30cm), or $\omega = 6.28\times10^9\, rad/s$ at several applied magnetic fields ranging from 1T to 4T [Fig. 1(b)]. At large DC magnetic field (> 3T), there exist two EFCs, one bounded (RH) and the other extending to infinity (LH), reminiscent of the EFCs of the transverse-electric-field (TE) and transverse-magnetic-field (TM) modes in a hyperbolic medium. For the magnetic field below a cut-off value (2.85T), the permittivity of RH mode becomes negative and its propagation is not supported in the plasma anymore. As a result, its EFC disappears at lower magnetic field of 1T and 2T in Fig. 1(b).

One naturally wonders whether the sub-diffraction imaging is enabled by the unbounded LH mode in the magnetized plasma, in a similar way as that in a hyperbolic medium. To investigate the strength of the magnetized plasma in imaging, we carried out numerical simulations on wave propagation with sub-diffraction features using a commercial software -- Comsol. The configuration is shown in Fig. 2. The object to be imaged consists of three holes, positioned in a triangle, with diameter of λ/7.5 and spacing of λ/5 in a PEC film, which is separated by λ/30 from the plasma. A plane electromagnetic wave of 1 GHz frequency is incident normal to the PEC film. The

plasma frequency is kept the same as before ($\omega_p = 5.64\times10^{10} rad/s$), whereas a very large collision frequency γ=5 GHz is assumed (two orders' of magnitudes larger than that in Ref. 16) to ensure the convergence of the simulation. The permittivity tensor taking into account the finite collision frequency is given by [17].

$$\varepsilon = 1 + \frac{i\omega_p^2}{\omega\gamma}\begin{pmatrix} \frac{1-i\omega/\gamma}{(1-i\omega/\gamma)^2+\omega_c^2/\gamma^2} & \frac{-\omega_c/\gamma}{(1-i\omega/\gamma)^2+\omega_c^2/\gamma^2} & 0 \\ \frac{\omega_c/\gamma}{(1-i\omega/\gamma)^2+\omega_c^2/\gamma^2} & \frac{1-i\omega/\gamma}{(1-i\omega/\gamma)^2+\omega_c^2/\gamma^2} & 0 \\ 0 & 0 & \frac{1}{1-i\omega/\gamma} \end{pmatrix} \quad (4)$$

The distribution of the electric field is shown in Fig. 3. The fields plot in the *x-z* plane presents a direct view on how the wave propagates inside the plasma [Fig. 3(a)]. At the lowest magnetic field of 1T, the waves emerging from the holes interfere and form a diffraction pattern after propagating through a certain distance. As a result, the pattern of the three holes is not transported to the image side, as shown in Fig. 3(b, c). However, it is worth noting that the sub-wavelength spatial information of the object is still contained in the diffraction pattern, as the waves with large in-plane wave vectors can propagate through the magnetized plasma. As the magnetic field increases, the electromagnetic waves start to exhibit almost diffraction-less propagation, and are confined in narrow beams with deep sub-wavelength width. This can be attributed to a flatter EFC at higher magnetic field (Fig. 1). Standing wave pattern is formed along the propagation due to the impedance mismatch at the plasma/air interface; similar effect has been observed and discussed for acoustic superimaging devices [18, 19]. Diffraction-less propagation is very important for the imaging, as illustrated by Fig. 3 (b, c), where three bright spots are clearly observed both inside and outside the plasma at higher magnetic fields of 3T and

4T, corresponding to the images of the three apertures in the PEC film. However, the images right outside the plasma in Fig. 3(b) are somewhat distorted, namely, the bright spots are slightly larger than the apertures, and the two bright spots aligned along *x* direction have slightly larger separation than the separation between the corresponding apertures. Whereas inside the plasma, the field plots faithfully exhibits the same pattern as the object [Fig. 3(c)]. The difference between the field plots inside and outside the plasma can be attributed to the large discontinuity of the z-component of the electric field at the interface between the plasma and air. This is confirmed by the plot of the x and z components of the electric field at 4T magnetic field in Fig. 4. Inside the plasma, the total electric field is dominated by the x component; in comparison, the z-component is almost negligible. Across the interface, the z-component of electric displacement field is continuous, and due to the large permittivity of the plasma along the surface normal, the z-component of the electric field outside the plasma is significantly larger than that inside the plasma, and comparable to the magnitude of x-component. Therefore, one possible solution for imaging would be a polarization selective detection wherein only the in-plane (x-y) component of the electric field is measured.

The imaging resolution of the magnetized plasma system is fundamentally limited by the material loss and thickness of the plasma. This is evident from the plot of $Im(k_z)$ vs k_x [Fig. 5(a)], obtained by combining Eqn. 4 and the wave equation, for a plasma under a magnetic field of 4 Tesla, and with a realistic colliding frequency of 30MHz taken from Ref. 16. The imaginary part of k_z increases linearly at large k_x, indicating that the waves containing information of higher spatial resolution experience higher propagating loss. The resolution is inversely proportional to the thickness of the

magnetized plasma d, as the attenuation is characterized by $e^{-Im(kz)d}$. Given a magnetized plasma with a thickness λ_0 as in the configuration shown in Fig. 2, the spatial resolution can be estimated by $Im(k_z)\lambda_0=1$, or $Im(k_z)/k_0=0.16$, which, according to Fig. 5(a), corresponds to an extremely large cut-off in-plane wave vector $k_x=585k_0$, or an imaging resolution of $\lambda_0/1170$=256μm! The inset of Fig. 5(a) shows $Im(k_z)/k_0=5\times10^{-4}$ for $k_x=4k_0$, which means that feature size of $\lambda_0/8$ can be transported through a plasma of $320\lambda_0$ thick. As shown by Fig. 5(b), even with an exaggerated collision frequency of 5 GHz, the cut-off in-plane wave-vector for imaging after a propagation length of λ_0 is given as $k_x=6k_0$, corresponding to an imaging resolution of $\lambda_0/12$. This is consistent with the simulation results shown in Fig. 3 and 4 where features as small as $\lambda_0/7.5$ can be resolved.

The imaging system based on magnetized plasma can be readily modified to curved configurations, with magnetic field approximately along the radial directions, to form a hyperlens [11]. In such a configuration, sub-diffractional object can be magnified through the magnetized plasma hyperlens, and imaged in the far field. The imaging can be dynamically tuned by varying the plasma density (plasma frequency), or the applied magnetic field magnitude and direction. Imaging with magnetized plasma can be extended to radio frequencies where important applications such as magnetic resonance imaging (MRI) may benefit from the capability of transportation and magnification of deep subwavelength features. In certain doped semiconductors such as Indium Antimonide (InSb), the effective mass of electrons is almost two orders of magnitude less than its free space mass; therefore, the cyclotron frequency can easily reach terahertz with readily available magnetic field. Thus, reconfigurable sub-diffraction imaging using magnetized plasma may bring important applications to the terahertz as well.

Captions:

Fig. 1. (a) Four critical parameters determining the dispersion of magnetized plasma, ε_R, ε_L, ε_P, and ε_X vs. electromagnetic frequency at an applied magnetic field of 4T. The vertical dashed line shows the frequency whereat the EFCs are plotted. **(b)** The EFCs of plasma under magnetic field ranging from 1 to 4 Tesla. The plasma density is $1\times10^{12}\,cm^{-3}$ (corresponding to $\omega_p = 5.7\times10^{10}\,rad/s$) and the electromagnetic frequency is 1 GHz, or $\omega = 6.28\times10^{9}\,rad/s$. There exist two EFCs for magnetic field at 3T and 4T, whereas the EFC of the right handed mode disappears at lower magnetic fields of 1T and 2T. The horizontal dashed lines in each figure assist to indicate flatness of the EFC of the left handed mode.

Fig. 2. Schematic of an imaging system based on the magnetized plasma. The object consists of three sub-wavelength circular apertures in a PEC film, with the detailed geometry shown in the figure. The magnetic field is along the z direction. A plane wave is incident upon the object at the normal direction from underneath the object, with the polarization indicated.

Fig. 3. The simulated field distribution at magnetic field ranging from 1T to 4T. In the calculation, a higher collision frequency is assumed to assure the convergence of the calculation. **(a)** field plot in an *x-z* plane that intercepts the centers of two holes aligned along *x* direction. **(b)** field plot in an *x-y* plane right outside the plasma on the image side (output plane). **(c)** field plot in an *x-y* plane inside the plasma at the anti-node of the standing wave, as indicated by the white dashed lines in (a).

Fig. 4. The field plots of the x- and z- components of the electric field at 4T magnetic field in the **(a)** x-z plane, and **(b)** x-y output plane.

Fig. 5. (a) plot of $Im(k_z)$ vs k_x for the same parameters as in Fig. 1, but with a realistic collision frequency of 30 MHz taken from Ref. 16. The inset shows a zoom-in view of the plot for k_x up to $5k_0$. **(b)** the same as (a) but with an exaggerated collision frequency of 5 GHz.

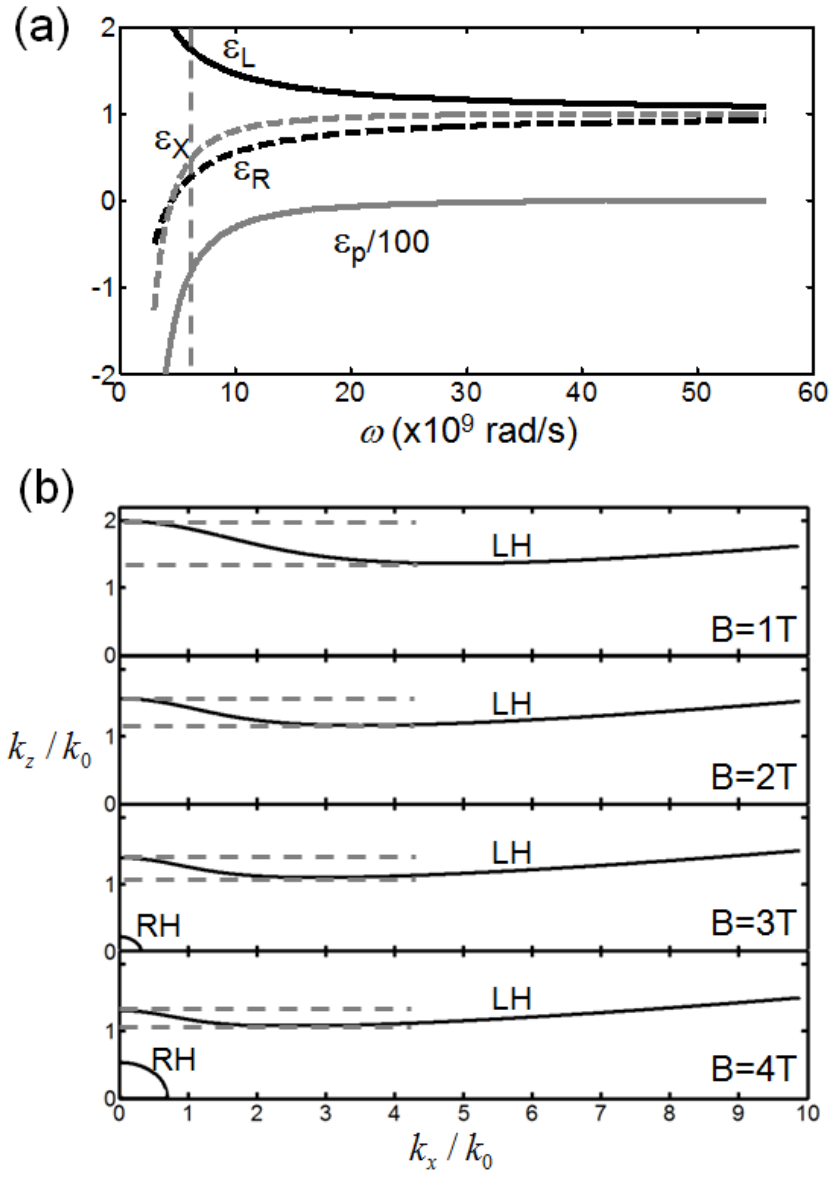
(a)
ε_L
ε_X
ε_R
$\varepsilon_p/100$
ω (x10^9 rad/s)
(b)
LH
B=1T
LH
B=2T
LH
RH
B=3T
LH
RH
B=4T
k_z / k_0
k_x / k_0

Fig. 1

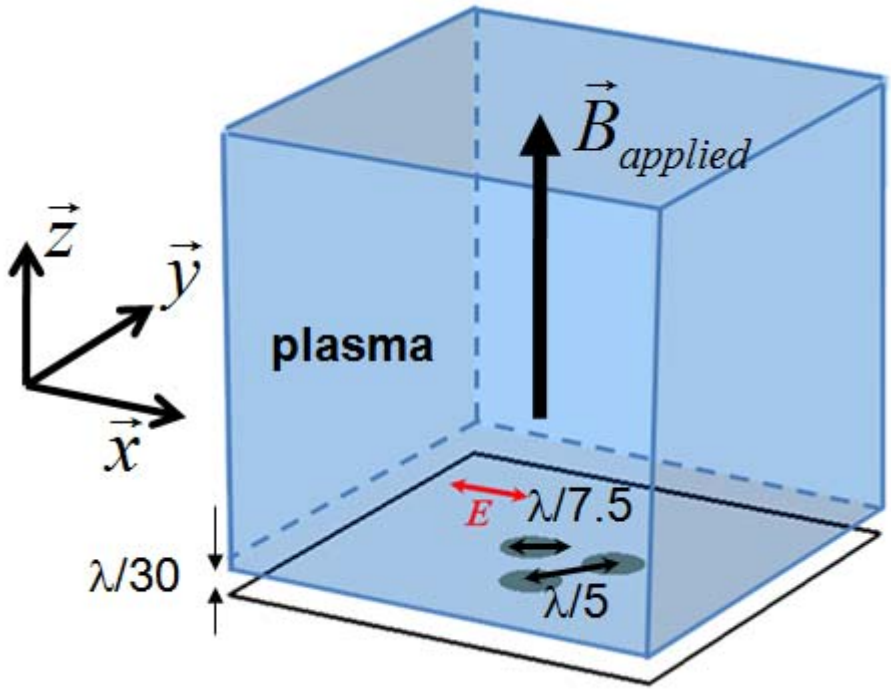

Fig. 2

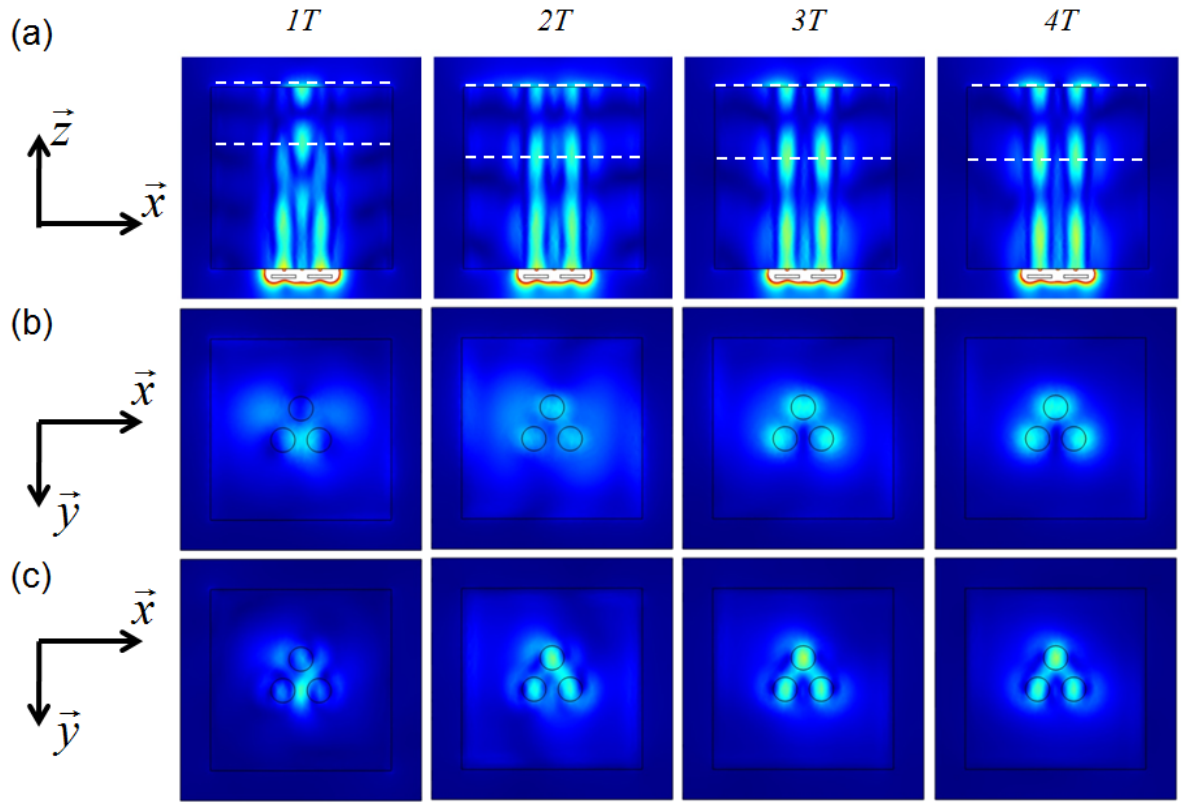

Fig. 3

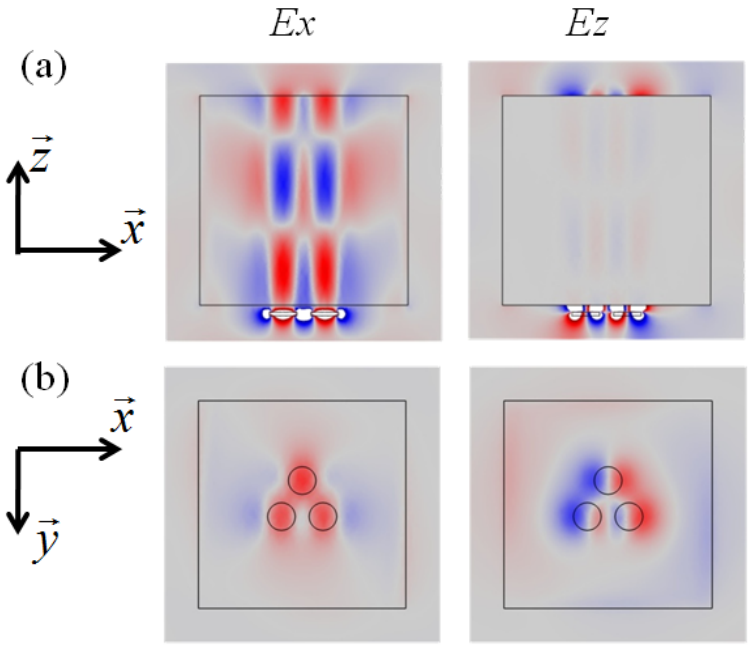

Fig. 4

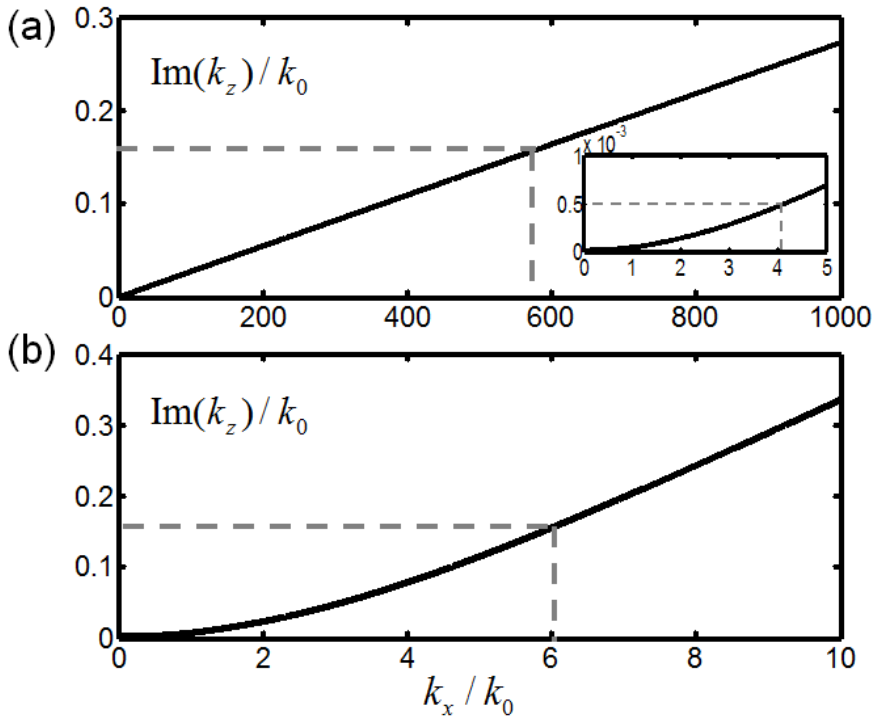
(a)
$\mathrm{Im}(k_z)/k_0$
0.3
0.2
0.1
0
0
200
400
600
800
1000
X 10^-3
1
0.5
0
0
1
2
3
4
5
(b)
$\mathrm{Im}(k_z)/k_0$
0.4
0.3
0.2
0.1
0
0
2
4
6
8
10
k_x/k_0

Fig. 5

1 V. G. Veselago, *Soviet Physics Uspekhi 10* (**4**): 509 (1968)

2 J. B. Pendry, *Phys. Rev. Lett.* **85**, 3966 (2000).

3 N. Fang, H. Lee, C. Sun & X. Zhang, *Science* **308** , 534 (2005).

4 T. Taubner et al, *Science* **313**, 1595 (2006)

5 J. B. Pendry, D. Schurig & D. R. Smith, *Science*, **312**, 1780 (2006)

6 D. Schurig et al, *Science* **314**, 977 (2006)

7 A. Grbic and G. V. Eleftheriades, *Phys. Rev. Lett.*, **92**, 117403 (2004).

8 D. R. Smith and D. Schurig, *Phys. Rev. Lett*. **90**, 077405 (2003).

9 Zubin Jacob et al, *Opt. Express* **14**, 8247 (2006)

10 A. Salandrino & N. Engheta, *Phys. Rev. B*, **74**, 075103 (2006)

11 Z. W. Liu et al, *Science*, **315**, 1686 (2007)

12 J. Yao et al, *Science*, **321**, 930 (2008)

13 P. A. Belov et al, *Phys. Rev. B*, **77**, 193108 (2008)

14 M. Wiltshire et al, *Science,* **291,** 849 (2001)

15 P. W. Bellan, *Fundamental of Plasma Physics* (Cambridge University Press, 2006)

16 Y. P. Bliokh, J. Felsteiner & Y. Z. Slutsker, *Phys. Rev. Lett.* **95**, 165003 (2005)

17 Y. M. Strelniker and David J. Bergman, *Phys. Rev. B.* **77**, 205113 (2008)

18 J. Li et al, Nature Materials, 8, 931 (2009)

19 J. Zhu et al, Nature Physics, 7, 52 (2011)